Hydrodynamics of polymers in an active bath

Aitor Martin-Gomez, Thomas Eisenstecken, Gerhard Gompper,* and Roland G. Winkler†
Theoretical Soft Matter and Biophysics, Institute of Complex Systems and Institute for Advanced Simulation, Forschungszentrum Jülich, 52425 Jülich, Germany

(Received 2 March 2020; accepted 30 April 2020; published 26 May 2020)

The conformational and dynamical properties of active polymers in solution are determined by the nature of the activity. Here, the behavior of polymers with self-propelled, active Brownian particle-type monomers differs qualitatively from that of polymers with monomers driven externally by colored-noise forces. We present simulation and theoretical results for polymers in solution in the presence of external active noise. In simulations, a semiflexible bead-spring chain is considered, in analytical calculations, a continuous linear wormlike chain. Activity is taken into account by independent monomer or site velocities, with orientations changing in a diffusive manner. In simulations, hydrodynamic interactions (HIs) are taken into account by the Rotne-Prager-Yamakawa tensor or by an implementation of the active polymer in the multiparticle-collision-dynamics approach for fluids. To arrive at an analytical solution, the preaveraged Oseen tensor is employed. The active process implies a dependence of the stationary-state properties on HIs via the polymer relaxation times. With increasing activity, HIs lead to an enhanced swelling of flexible polymers, and the conformational properties differ substantially from those of polymers with self-propelled monomers in the presence of HIs, or free-draining polymers. The polymer mean-square displacement is enhanced by HIs. Over a wide range of timescales, hydrodynamics leads to a subdiffusive regime of the site mean-square displacement for flexible active polymers, with an exponent of $5/7$, larger than that of the Rouse ($1/2$) and Zimm ($2/3$) models of passive polymers.

DOI: 10.1103/PhysRevE.101.052612

I. INTRODUCTION

Active matter is characterized by a continuous energy consumption of its agents from internal or external sources, which can be converted into directed motion [1]. The associated out-of-equilibrium nature of active matter is the origin of fascinating phenomena, such as activity-driven phase separation or large-scale collective motion, aspects absent in corresponding passive systems [1–6]. A simple and generic model for a dry-active-matter agent [7] is the active Brownian particle (ABP), a hard-sphere- or hard-disk-type particle propelled in a body-fixed direction, which changes in a diffusive manner [1,3,4,8–16]. Computer simulations of ABP ensembles reveal motility-induced phase separation (MIPS) [3,4,9–15], enhanced wall accumulation [11,16,17], and an active pressure (denoted as swim pressure) [18–22]. Additional fascinating structural and dynamical properties can be expected from more complex assemblies of active particles, such as dumbbells [23–29], linear polymers [30–49], or other arrangements [50]. The coupling of activity and internal degrees of freedom gives rise to novel phenomena, such as an activity-induced polymer collapse, typical in two dimensions, [31,32,47] or swelling [32,33,38,42,44,46,51], and a polymer-length-dependent suppression of phase separation [24,27]. This illustrates that active soft matter is a promising new class of materials with many as yet unexplored features [52,53].

Nature provides a wide spectrum of systems, where properties are governed by the activity of filamentous, polymer-like building blocks and structures. Linear polymers, such as filamentous actin or microtubules of the cell cytoskeleton are propelled by tread-milling and motor proteins [2,54–59]. Similarly, in motility assays, filaments are propelled on carpets of motor proteins anchored on a substrate [60–63]. Moreover, the active dynamics of microtubules [64] or actin-filaments [65] enhances the dynamics of chromosomal loci [66,67] and chromatin [68]. A characteristic feature of biological cells is the intrinsic mixture of active and passive components; specifically the active cytoskeleton and a large variety of passive colloidal and polymeric objects [46,69]. Due to an accelerated dynamics of the stirred fluid in the cytoskeleton, a large variety of embedded objects, such as vesicles, passive colloids, polymeric structures, experience an enhanced stochastic motion, which implies an enhanced random motion of tracer particles. Similarly, countless ATP-dependent enzymatic activity-induced mechanical fluctuations drive molecular motion in the bacterial cytoplasm and the nucleus of eukaryotic cells [66]. Moreover, self-propelled long swarming bacteria, such as *Proteus mirabilis* in biofilms [70], appear as semiflexible polymers, and rodlike objects are formed via self-assembly, e.g., by dinoflagellates [71,72].

Synthetic active or activated colloidal polymers [48] are nowadays synthesized in various ways. Assembly of active chains of metal-dielectric Janus colloids (monomers) can be achieved by imbalanced interactions, where simultaneously the motility and the colloid interactions are controlled by an AC electric field [73–75]. Electrohydrodynamic convection

*g.gompper@fz-juelich.de
†r.winkler@fz-juelich.de

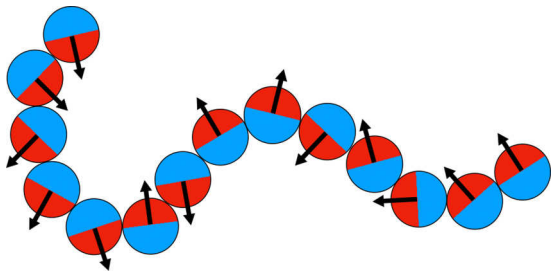

FIG. 1. Illustration of an active polymer. ABP monomers are drive by persistent forces (indicated by arrows) whose temporal orientation correlations decay exponentially.

rolls lead to self-assembled colloidal chains in a nematic liquid crystal matrix and directed movement [76]. Moreover, chains of linked colloids, which are uniformly coated with catalytic nanoparticles, have been synthesizes [77]. Hydrogen peroxide decomposition on the surfaces of the colloidal monomers generates phoretic flows, and active hydrodynamic interactions between monomers results in an enhanced diffusive motion [77].

Hydrodynamic interactions (HIs) play a major role for the conformational and dynamical properties of active polymers. As has been shown in simulations, the hydrodynamic coupling between two polar externally driven filaments leads to cooperative effects [36]. Polymers composed of self-propelled ABPs shrink substantially in the presence of HIs at moderate activities and swell at high activity [78], however, far less extent than dry active polymers [42,44].

In this article, we explore the effect of external colored noise, mimicking an active environment, on the properties of semiflexible polymers in dilute solution by hydrodynamic simulations and analytical theory. These kinds of active polymers are different from polymers with self-propelled monomers [48,78], as the active contribution is not force free, but active forces give rise to Stokeslet flows. We analyze the influence of the additional hydrodynamic flow field on the conformational and dynamical polymer properties, in comparison to self-propelled polymers. We like to emphasize that in the absence of HIs, the properties of active polymers with externally driven and self-propelled monomers are identical [42].

In simulations, the polymers are described as bead-spring linear phantom or self-avoiding chains with ABP-type monomers (cf. Fig. 1), which change their propulsion direction in a diffusive manner [42]. Hydrodynamic interactions are taken into account through the Rotne-Prager-Yamakawa hydrodynamic tensor [79,80]. Alternatively, the same polymers are embedded in a multiparticle-collision dynamics fluid [81,82]. The Gaussian semiflexible polymer model is adopted for the analytical considerations [42,83,84], with active sites modeled by an Ornstein-Uhlenbeck process [active Ornstein-Uhlenbeck particle (AOUP)] [16,42,85], where the active velocity vector changes in a diffusive manner; here the HIs are included via the preaveraged Oseen tensor [86]. Monomer Stokeslets arise from bond, bending, and excluded-volume interactions between monomers, from thermal forces, and, in particular, from active forces. Hence, we capture the long-range character of HIs in polymers of a broad class of externally driven active monomers.

Our studies reveal a decisive influence of hydrodynamic interactions on the active polymer conformations and dynamics. Externally driven flexible polymers monotonically swell with increasing activity, in contrast to polymers with self-propelled monomers [78]. Semiflexible polymers shrink at moderated activities and swell for high activities. In the asymptotic limit of large activities, the same stretching as for free-draining active polymers is observed. The reason is the violation of the fluctuation-dissipation theorem of the active processes, which leads to the dependence of stationary-state properties on the hydrodynamically modified relaxation times, however, in a different and less dominant way as for polymers of self-propelled monomers. The particular conformations are a consequence of the timescale separation between the thermal processes, dominating for zero or very weak activities, and the active processes with hydrodynamically slowed-down relaxation times. The activity-dependent relaxation times also affect the translation motion, and a subdiffusive time regime appears, where the monomer mean-square displacement (MSD) in the polymer center-of-mass reference frame exhibits a power-law dependence with the exponent $\gamma' = 5/7$, larger than the Zimm value $\gamma' = 2/3$ of a passive polymer.

The manuscript is organized as follows. Section II describes the discrete model of the active polymer along with the simulation approaches. The results of the simulations are presented in Sec. III. The analytical approach is introduced in Sec. IV. Analytical results for the conformational and dynamical properties are discussed in Sec. V and Sec. VI, respectively. Finally, Sec. VII summarizes our findings. The Appendix provides asymptotic results for the stretching coefficient.

II. COMPUTER SIMULATIONS

A. Model of active polymers

The semiflexible polymers are composed of N_m active Brownian particles ($i = 1, \ldots, N_m$), which are linearly connected by a harmonic bond potential, U_l, and experience bond-orientational restrictions by the bending potential U_b. Excluded-volume interactions are taken into account by the purely repulsive Lennard-Jones potential U_{LJ}. Explicitly, the potentials are [78]

$$U_l = \frac{\kappa_l}{2} \sum_{i=2}^{N_m} (|\boldsymbol{R}_i| - l)^2, \tag{1}$$

$$U_b = \frac{\kappa_b}{2} \sum_{i=2}^{N_m-1} (\boldsymbol{R}_{i+1} - \boldsymbol{R}_i)^2, \tag{2}$$

$$U_{LJ} = \begin{cases} 4\epsilon \sum_{i<j} \left[\left(\frac{\sigma}{r_{ij}}\right)^{12} - \left(\frac{\sigma}{r_{ij}}\right)^{6} + \frac{1}{4} \right], & r_{ij} < \sqrt[6]{2}\sigma \\ 0, & r_{ij} > \sqrt[6]{2}\sigma \end{cases}. \tag{3}$$

The coefficients κ_l and κ_b are the bond and bending constants, respectively, and l is the equilibrium length of the bond vector $\boldsymbol{R}_{i+1} = \boldsymbol{r}_{i+1} - \boldsymbol{r}_i$. The vector $\boldsymbol{r}_{ij} = \boldsymbol{r}_i - \boldsymbol{r}_j$ is the vector between monomers i and j, and $r_{ij} = |\boldsymbol{r}_{ij}|$. The energy ϵ

measures the strength of the repulsive potential and σ defines the particle diameter. In addition, every monomer experience an active force

$$\boldsymbol{F}_i^a = F^a \boldsymbol{e}_i(t) \tag{4}$$

of constant magnitude F^a. We consider this as an external force in contrast to the self-propulsion force of Ref. [78]. As a consequence, an individual monomer in a fluid is no longer active force free, but the latter gives rise to a Stokeslet [1]. In any case—for polymers with self-propelled or externally driven monomers—Stokeslets appear by the forces of the potentials (1)–(3) and thermal noise. As for an active Brownian particle, we set $F^a = \gamma v_0$, with the friction coefficient $\gamma = 3\pi\eta d_H$ of the surrounding fluid—η is the fluid viscosity and d_H the monomer hydrodynamic diameter—and the active velocity v_0. The orientation $\boldsymbol{e}_i$ changes in a diffusive manner according to

$$\dot{\boldsymbol{e}}_i(t) = \hat{\boldsymbol{\eta}}_i(t) \times \boldsymbol{e}_i(t), \tag{5}$$

where $\hat{\boldsymbol{\eta}}_i$ is a Gaussian and Markovian stochastic processes with zero mean and the second moments

$$\langle \hat{\eta}_{i\alpha}(t)\hat{\eta}_{j\beta}(t')\rangle = 2D_R\delta_{\alpha\beta}\delta_{ij}\delta(t-t'). \tag{6}$$

Here T denotes the temperature, k_B the Boltzmann constant, D_R the rotational diffusion coefficient of a spherical colloid of diameter d_H, and $\alpha, \beta \in \{x, y, z\}$ refer to the axis of the Cartesian reference frame.

Fluid-mediated interactions are incorporated implicitly by the Rotne-Prager-Yamakawa (RPY) hydrodynamic tensor [79,80] or explicitly by modeling the fluid via the MPC approach [81,82].

B. Brownian dynamics with the RPY tensor

In Brownian dynamics simulations in the presence of hydrodynamic interactions, the overdamped equations of motion

$$\dot{\boldsymbol{r}}_i(t) = \sum_{j=1}^{N_m} \mathbf{H}_{ij}\left[\boldsymbol{F}_j^a + \boldsymbol{F}_j + \boldsymbol{\Gamma}_j(t)\right] \tag{7}$$

are considered. The forces $\boldsymbol{F}_i = -\nabla_{\boldsymbol{r}_i}(U_l + U_b + U_{LJ})$ follow from the potentials (1)–(3), and $\boldsymbol{\Gamma}_i$ accounts for thermal fluctuations. The random force $\boldsymbol{\Gamma}_i$ is modeled as a Gaussian and Markovian stochastic processes with zero mean and the second moments

$$\left\langle \boldsymbol{\Gamma}_i(t)\boldsymbol{\Gamma}_j^T(t')\right\rangle = 2k_BT\mathbf{H}_{ij}^{-1}\delta(t-t'), \tag{8}$$

where $\boldsymbol{\Gamma}_i^T$ denotes the transpose of $\boldsymbol{\Gamma}_i$ and $\mathbf{H}_{ij}^{-1}$ the inverse of $\mathbf{H}_{ij}$. The hydrodynamic tensor, $\mathbf{H}_{ij}(\boldsymbol{r}_{ij})$, is given by

$$\mathbf{H}_{ij}(\boldsymbol{r}_{ij}) = \frac{\delta_{ij}}{3\pi\eta d_H}\mathbf{I} + (1-\delta_{ij})\boldsymbol{\Omega}(\boldsymbol{r}_{ij}), \tag{9}$$

where the first term on the right-hand side accounts for local friction and the RPY tensor $\boldsymbol{\Omega}(\boldsymbol{r}_{ij})$ for interparticle interactions [78,86]. The RPY tensor ensures the positive definiteness of the hydrodynamic tensor even at small distances. The translational equations of motion (7) are solved via the Ermak-McCammon algorithm [87]. The procedure to solve the equations of motion (5) for the orientation vector is described in Ref. [20].

The active noise is quantified by the dimensionless Péclet number [16,42]

$$\mathrm{Pe} = \frac{v_0}{lD_R}, \tag{10}$$

which compares the time for the reorientation of an ABP monomer with that for its translation with velocity v_0 over the monomer radius. The ratio between translational, $D_T = k_BT/3\pi\eta d_H$, and rotational diffusion, D_R, of a single monomer is denoted as

$$\Delta = \frac{D_T}{d_H^2 D_R}. \tag{11}$$

In the following, we will always consider $\Delta = 0.6$. The coefficient κ_l [Eq. (1)] for the bond strength is adjusted according to the applied Péclet number, in order to avoid bond stretching with increasing activity. By choosing $\kappa_l l^2/k_BT = (10 + 2\mathrm{Pe})10^3$, bond-length variations are smaller than 3% of the equilibrium value l. Furthermore, the scaled bending force coefficient $\tilde{\kappa}_b = \kappa_b l^2/k_BT$ [Eq. (2)] is related to the polymer persistence length, $l_p = 1/(2p)$, by

$$pL = N_m \frac{\tilde{\kappa}_b[1-\coth(\tilde{\kappa}_b)]+1}{\tilde{\kappa}_b[1+\coth(\tilde{\kappa}_b)]-1}. \tag{12}$$

The parameters of the truncated and shifted Lennard-Jones potential are $\sigma = 0.8l$ and $\epsilon = k_BT$.

C. Active polymers in MPC fluid

1. Polymer dynamics

Every monomer is exposed to an active forces $\boldsymbol{F}_i^a = v_0\boldsymbol{e}_i(t)$ (4), hence, a polymer experiences the total external force

$$\boldsymbol{F}^a = \sum_{i=1}^{N_m} \gamma v_0 \boldsymbol{e}_i(t) = \frac{\mathrm{Pe}}{d_H\Delta}\sum_{i=1}^{N_m}\boldsymbol{e}_i(t), \tag{13}$$

which drags along fluid and induces an overall fluid flow [88]. In a confined systems, walls prevent global flow and give rise to fluid backflow. To prevent a net fluid flow in our system with periodic boundary conditions, we modify the equations of motion of the fluid (and the embedded polymer) in such a way that the total momentum of the system (fluid plus polymer) vanishes [88]. This implies the backflow force on a monomer:

$$\boldsymbol{F}_i^b = -\frac{M}{mN + MN_m}\boldsymbol{F}^a, \tag{14}$$

where m is the mass of a fluid particle, N is the total number of fluid particles, and M is the mass of a monomer. The dynamics of a monomer is then described by the equation of motion

$$M\ddot{\boldsymbol{r}}_i = \boldsymbol{F}_i + \boldsymbol{F}_i^a + \boldsymbol{F}_i^b, \tag{15}$$

with the force $\boldsymbol{F}_i$ following from the potentials (1)-(3). Equation (15) is solved by applying the velocity-Verlet algorithm.

2. Fluid dynamics and fluid-polymer coupling

The dynamics of the MPC fluid proceeds in two steps—streaming and collision [81,82]. In the steaming step, Newton's equations of motion for fluid particles are solved in the presence of the backflow force $m\boldsymbol{F}_i^b/M$ over a time interval

h, denote as collision time. Since $\boldsymbol{e}_i(t)$ changes very slowly in the time interval h for small diffusion coefficients D_R, we apply the integration scheme

$$\boldsymbol{v}_k(t+h) = \boldsymbol{v}_k(t) - \frac{h}{mN + MN_m}\boldsymbol{F}^a(t), \tag{16}$$

$$\boldsymbol{r}_k(t+h) = \boldsymbol{r}_k(t) + h\boldsymbol{v}_k(t) - \frac{h^2}{2(mN + MN_m)}\boldsymbol{F}^a(t), \tag{17}$$

where $\boldsymbol{r}_k(t)$ and $\boldsymbol{v}_k(t)$ are the position and velocity of the MPC particle k at time t, respectively. In the collision step, particles are sorted into cubic cells of side length a of a cubic, periodic systems of volume $V = Na^3/\langle N_c\rangle$ to define the collision environment; $\langle N_c\rangle$ is the mean number of fluid particles in a collision cell. Subsequently, the relative velocity of each particle, with respect to the center-of-mass velocity of all the particles within the corresponding collision cell, is rotated by a constant angle α around an arbitrarily orientated axis. The orientation of the rotation axis is chosen randomly and independently for every cell and collision step. Hence, the final velocity after a MPC step is

$$\boldsymbol{v}_k(t) = \boldsymbol{v}_{cm}(t) + \mathbf{R}(\alpha)[\boldsymbol{v}_k(t) - \boldsymbol{v}_{cm}(t)], \tag{18}$$

where $\mathbf{R}(\alpha)$ is the rotation matrix, and

$$\boldsymbol{v}_{cm}(t) = \frac{\sum_{k=1}^{N_c} m\boldsymbol{v}_k(t) + \sum_{j=1}^{N_m^c} M\boldsymbol{v}_j(t)}{mN_c + MN_m^c} \tag{19}$$

is the center-of-mass velocity of the N_c MPC particles and the N_m^c monomers within the cell of particle k. Similarly to Eq. (18), the velocities of the monomers are rotated, which yields the fluid-monomer coupling by MPC collisions.

Partitioning of space in collision cells implies violation of Galilean invariance, which is reinstalled by a random shift of the collision lattice at every collision step [82,89]. In order to maintain locally a constant temperature, the Maxwell-Boltzmann scaling method is applied [90].

We measure energies in units of k_BT, lengths in units of the collision cell $a = l$, which is set equal to the equilibrium bond length, and time in units of $\tau = \sqrt{ma^2/k_BT}$. The MPC particle mass is set to $m = 1$, the monomer mass to $M = 10m$, the average number of particles in a collision cell to $\langle N_c\rangle = 10$, and $\epsilon = k_BT$. A time step $h = 0.01\sqrt{ma^2/k_BT}$ is used, which corresponds to the viscosity $\eta = 82.14\sqrt{mk_BT/a^4}$ [91]. MPC is an ideal gas and, hence, its isothermal velocity of sound is $c_T = \sqrt{k_BT/m}$, which is unity in the units of the simulation. To realize low Mach numbers, the transport velocity of an active monomer has to be small compared to c_T. All simulations are performed in a cubic periodic box of linear size $L_B = 100a$.

In order to compare simulation results obtained via the MPC approach with the Brownian dynamics simulations using the RPY tensor, several parameters have to be adjusted. In particular, MPC simulations yield the hydrodynamic diameter $d_H = 0.6a$ of a monomer [92,93], which yields, with $D_R = 100/\tau$, $\Delta = k_BT/(3\pi\eta d_H^3 D_R) \approx 0.6$.

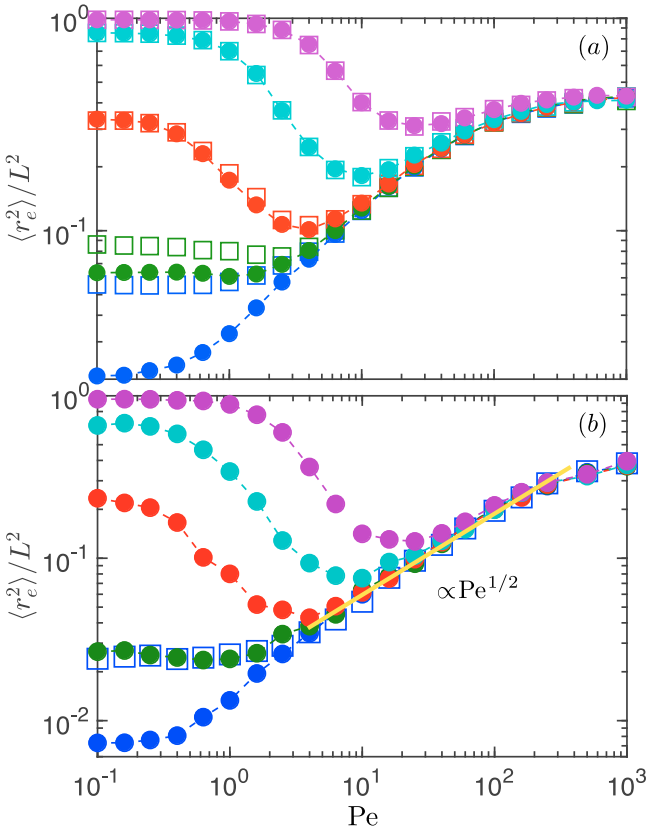

FIG. 2. Polymer mean-square end-to-end distance as a function of the Péclet number for semiflexible polymers with (a) $N_m = 50$ ($L = 49l$) and (b) $N_m = 150$ ($L = 149l$) monomers. Bullets are results of phantom polymers and squares results of self-avoiding polymers in (a) for $pL = 5 \times 10^1$ (blue), 1.5×10^1 (green), 2.6 (red), 2.5×10^{-1} (cyan), and 2.5×10^{-2} (purple), and in (b) for $pL = 1.5 \times 10^2$ (blue), 4.5×10^1 (green), 7.5 (red), 7.5×10^{-1} (cyan), and 7.5×10^{-2} (purple) (bottom to top). The dashed lines are guides for the eye. The solid line (yellow) in (b) indicates a power-law dependence in the respective regime. Hydrodynamics is taken into account by the RPY hydrodynamic tensor.

III. COMPUTER SIMULATIONS: RESULTS

A. Conformational properties

The average shape of the polymers is characterized by their mean-square end-to-end distance. Figure 2 displays results for phantom and self-avoiding polymers of lengths $L = (N_m - 1)l = 49l$, $149l$ and various persistence lengths $l_p = 1/(2p)$. Evidently, flexible polymers, with $pL \gg 1$, swell monotonically with increasing Péclet number, whereas semiflexible polymers shrink at moderate Pe, and swell for large Pe similarly as flexible polymers. In the asymptotic limit $\mathrm{Pe} \to \infty$, the value $\langle \boldsymbol{r}_e^2\rangle \approx 2L^2/5$ is assumed. Excluded-volume interactions change the behavior in so far as $\langle \boldsymbol{r}_e^2\rangle/L^2$ starts at a larger equilibrium value [cf. Fig. 2(a)]. For higher Pe and swollen polymers, self-avoidance becomes irrelevant. A qualitative similar behavior is obtained for longer polymers, only quantitative differences appear [cf. Fig. 2(b)]. However, longer polymers exhibit the universal, persistence-length independent increase $\langle \boldsymbol{r}_e^2\rangle \sim \mathrm{Pe}^{1/2}$ with increasing Pe above a critical value. This regime appears for sufficiently long

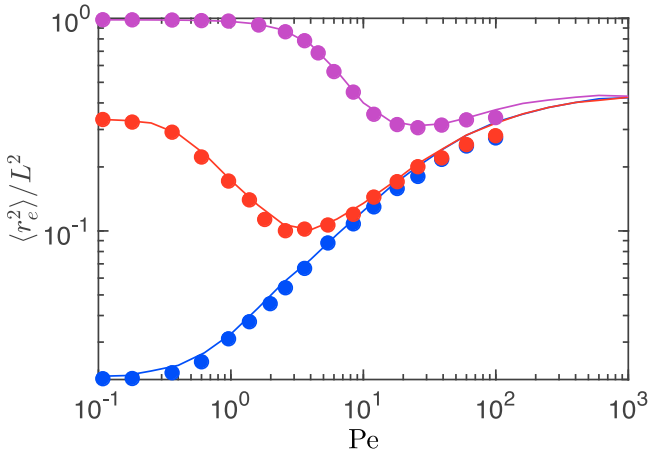

FIG. 3. Polymer mean-square end-to-end distance as a function of the Péclet number of semiflexible polymers with $N_m = 50$ ($L = 49l$) monomers for $pL = 5 \times 10^1$ (blue), 2.6 (red), and 2.5×10^{-2} (purple) (bottom to top). Solid lines are results applying the RPY tensor, and bullets are results of hydride simulations using the MPC approach.

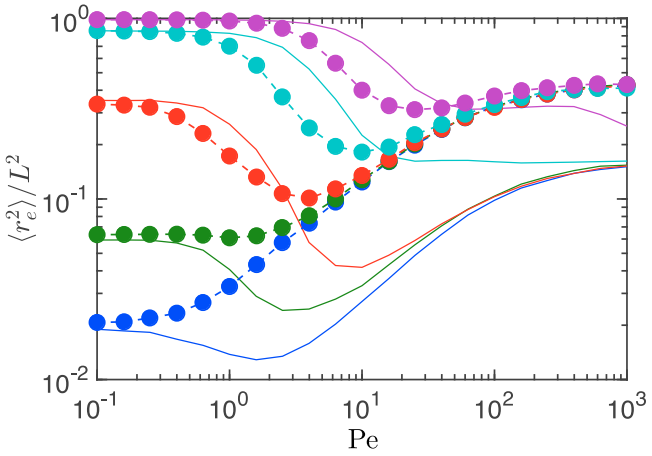

FIG. 4. Polymer mean-square end-to-end distance as a function of the Péclet number of semiflexible polymers of length $N_m = 50$ ($L = 49l$) and $pL = 5 \times 10^1$ (blue), 1.5×10^1 (green), 2.6 (red), 2.5×10^{-1} (cyan), and 2.5×10^{-2} (purple) (bottom to top). Bullets indicate results for the external active process and solid lines the respective results for self-propelled monomers (ABPO + HI [78]). Hydrodynamics is taken into account by the RPY hydrodynamic tensor.

polymers only and is not present for $N_m = 50$. In addition, a nonuniversal cross-over regime exists for flexible polymers in the range $5 \lesssim \mathrm{Pe} \lesssim 30$. These regimes and the observed Pe dependence of the universal regime are explained by the theoretical model in Sec. V.

The mean-square end-to-end distances obtained for polymers embedded in a MPC solvent are compared with the simulation results applying the RPY tensor in Fig. 3. Good quantitative agreement of the polymer conformations for the two simulation approaches is obtained, which confirms their suitability for these simulation studies. For the hybrid MPC approach, deviations from the RPY tensor simulations appear for $\mathrm{Pe} \gtrsim 10^2$. This is attributed to limitations of the MPC approach in terms of Mach and Reynolds numbers. The range of Péclet number can be extended by applying a smaller collision time step and/or by a higher mean value of MPC particles in a collision cell.

The structural properties of the polymer in the presence of hydrodynamic interactions strongly depends on the nature of the active process. As discussed in Sec. II A, the active force is considered here as an external force, mimicking an active environment. Figure 4 shows that such an external active force leads to a significantly stronger polymer swelling than intrinsic self-propulsion (cf. Ref. [78]). Remarkably, in contrast to the shrinkage of flexible active polymers with self-propelled monomers over a range of Péclet numbers, flexible externally driven active polymers monotonically swell. Moreover, the externally driven active polymers assume a larger asymptotic mean-square end-to-end distance for $\mathrm{Pe} \to \infty$, i.e., intrinsically active Brownian polymers in the presence of hydrodynamic interactions are more compact. We will provide a qualitative and quantitative explanation for these observations in Sec. V.

B. Dynamical properties

The effect of activity on the polymer dynamics is illustrated in Fig. 5, which displays the average monomer mean-square displacement

$$\overline{\langle \Delta \boldsymbol{r}^2(t)\rangle} = \frac{1}{N_m}\sum_{i=1}^{N_m}\langle[\boldsymbol{r}_i(t) - \boldsymbol{r}_i(0)]^2\rangle. \tag{20}$$

A passive polymer exhibits the well-known Zimm behavior for $t/\tilde{\tau}_1 \ll 1$, with the time dependence $t^{2/3}$ of the MSD in the center-of-mass reference frame, where $\tilde{\tau}_1$ is the longest polymer relaxation time in the presence of HIs [86]. In the

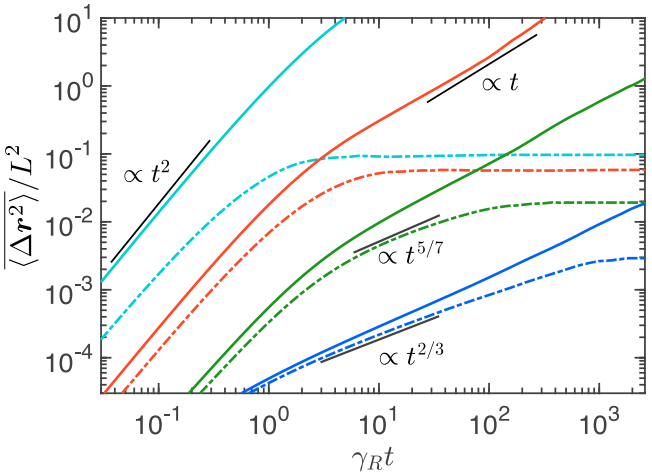

FIG. 5. Mean-square displacement of flexible polymers with $N_m = 150$ ($pL = 150$) monomers for the Péclet numbers $\mathrm{Pe} = 0$ (blue), 10^1 (green), 10^2 (red), and 10^3 (cyan) (bottom to top). The time is scaled by the factor $\gamma_R = 2D_R$. The solid lines indicate the overall monomer MSD and the dashed lines their MSD in the polymer center-of-mass reference frame. The short lines (black) indicating a power-law dependence of the data in the respective regime. Hydrodynamics is taken into account by the RPY hydrodynamic tensor.

asymptotic limit $t \to \infty$, the MSD depends linearly on time, with an activity-dependent diffusion coefficient (cf. Sec. VI). At large activities, the MSD exhibits a ballistic regime for short times, similar to a single ABP [1], but with the reduced (average) velocity $v_0/\sqrt{N_m}$ [cf. Eq. (56)]. Due to the independence of the monomer rotational motion, the effective center-of-mass ballistic velocity is determined by the fluctuations of the monomer propulsion direction, which yields the factor $1/\sqrt{N_m}$. In the center-of-mass reference frame, the monomer MSD exhibits a subdiffusive power-law regime for Pe ≈ 10, with an activity-determined effective exponent of $5/7$ (cf. Sec. VI for a derivation of the exponent). This regime extents with polymer length, but becomes smaller with increasing Pe, since the relaxation time $\tilde{\tau}_1$ decreases with increasing Péclet number. Nevertheless, it is a consequence of hydrodynamic interactions and activity (cf. Sec. VI for a more detailed discussion).

IV. ANALYTICAL APPROACH

Insight into the qualitative differences between externally driven active polymers and polymers composed of self-propelled monomers is achieved by an analytical model, where the polymers are described as continuous Gaussian semiflexible chains. This model has previously been applied to linear and ring active Brownian free-draining polymers [42,44,46,51,94], as well as to linear self-propelled polymers with hydrodynamic interactions [78].

A. Model and equations of motion

The polymers are considered as differentiable space curves $\boldsymbol{r}(s,t)$ of total length L, with contour coordinate s ($-L/2 \leqslant s \leqslant L/2$), and their conformations change with time t. The external active process is introduced by assigning an independent velocity $\boldsymbol{v}(s,t)$ to every site $\boldsymbol{r}(s,t)$. The corresponding Langevin equation is [84,95]

$$\frac{\partial \boldsymbol{r}(s,t)}{\partial t} = \int_{-L/2}^{L/2} ds' \, \mathbf{H}(\boldsymbol{r}(s),\boldsymbol{r}(s'))\Big[3\pi\eta \boldsymbol{v}(s',t) + 2\nu k_B T \frac{\partial^2 \boldsymbol{r}(s',t)}{\partial s'^2} - \epsilon k_B T \frac{\partial^4 \boldsymbol{r}(s',t)}{\partial s'^4} + \boldsymbol{\Gamma}(s',t)\Big]. \tag{21}$$

Free-end boundary conditions are applied as described in Refs. [42,96]. Moreover, the constraint on the (average) contour length

$$\int_{-L/2}^{L/2} ds \left\langle \left[\frac{\partial \boldsymbol{r}(s,t)}{\partial s}\right]^2 \right\rangle = L \tag{22}$$

is take into account, which is fundamental to achieve the correct polymer properties [42,51,96]. The tensor

$$\mathbf{H}(\boldsymbol{r}(s),\boldsymbol{r}(s')) = \frac{\delta(s-s')}{3\pi\eta}\mathbf{I} + \boldsymbol{\Omega}(\boldsymbol{r}(s)-\boldsymbol{r}(s')) \tag{23}$$

captures the hydrodynamic interactions, where the first term on the right-hand side describes the local friction, and

$$\boldsymbol{\Omega}(\Delta\boldsymbol{r}) = \frac{1}{8\pi\eta|\Delta\boldsymbol{r}|}\left(\mathbf{I} + \frac{\Delta\boldsymbol{r}\otimes\Delta\boldsymbol{r}}{|\Delta\boldsymbol{r}|^2}\right) \tag{24}$$

is the Oseen tensor [78,86]. The terms in Eq. (21) with the second and forth derivative capture chain flexibility, i.e., chain entropy, and bending forces, respectively. The Lagrangian multiplier ν accounts for the inextensibility of the polymer (we will denote ν as stretching coefficient in the following) and ϵ characterizes the bending stiffness [83,97]. For a polymer in three dimensions, previous studies yield $\epsilon = 3/4p$ [83,97].

For the velocity $\boldsymbol{v}(s,t)$, we adopt a non-Markovian Gaussian stochastic processes with zero mean and the correlation function (colored noise)

$$\langle \boldsymbol{v}(s,t)\cdot\boldsymbol{v}(s',t')\rangle = v_0^2 l e^{-\gamma_R|t-t'|}\delta(s-s'). \tag{25}$$

This correlation function follows from Eq. (5) or, similarly, by considering a monomer as an active Ornstein-Uhlenbeck particle (AOUP) [1,16,26,41,42].

As outlined in Sec. II A, $\boldsymbol{v}(s,t)$ is a consequence of an external forcing, hence $\boldsymbol{v}(s,t)$ appears inside the integral in Eq. (21) and implies a Stokeslet flow.

B. Solution of the equations of motion

1. Hydrodynamic tensor: Preaveraging approximation

In order to find an approximate analytical solution of the nonlinear and nonlocal equation of motion (21), we apply the preaveraging approximation, where the hydrodynamic tensor $\mathbf{H}(\boldsymbol{r}(s)-\boldsymbol{r}(s'))$ is replaced by its stationary-state average, i.e., $\mathbf{H}(\boldsymbol{r}(s)-\boldsymbol{r}(s')) \to \langle \mathbf{H}(\boldsymbol{r}(s)-\boldsymbol{r}(s'))\rangle = \mathbf{H}(s,s')$ [84,86]. Hence, Eq. (21) turns into a linear equation (Ornstein-Uhlenbeck process) with a Gaussian stationary-state distribution function for the distance $\Delta\boldsymbol{r}(s,s') = \boldsymbol{r}(s)-\boldsymbol{r}(s')$ of the form [16,84,86]

$$\Psi(\Delta\boldsymbol{r}) = \left[\frac{3}{2\pi a^2(s,s')}\right]^{3/2} \exp\left[-\frac{3\Delta\boldsymbol{r}^2}{2a^2(s,s')}\right], \tag{26}$$

with $a^2(s,s') = \langle[\boldsymbol{r}(s)-\boldsymbol{r}(s')]^2\rangle$. Then the Oseen tensor (24) becomes

$$\boldsymbol{\Omega}(s,s') = \frac{\Theta(|s-s'|-d_H)}{3\pi\eta}\sqrt{\frac{3}{2\pi a^2}}\mathbf{I} = \Omega(s,s')\mathbf{I}. \tag{27}$$

The Heaviside step function $\Theta(x)$ introduces d_H as a lower cutoff for the hydrodynamic interactions, which can be identified with the thickness of the polymer.

The preaveraging approximation has very successfully been applied to describe the dynamics of DNA [95] and semiflexible polymers [84]. Even quantitative agreement between analytical theory and simulations of the full hydrodynamic contribution of rather stiff polymers is achieved [98], as well as with measurements on DNA [95]. This demonstrates the suitability of preaveraging even for stretched polymers. However, the preaveraging approximation overestimates the hydrodynamics of rodlike objects [99].

2. Eigenfunction expansion

The linearized equation of motion is solved by the eigenfunction expansion

$$\boldsymbol{r}(s,t) = \sum_{n=0}^{\infty} \boldsymbol{\chi}_n(t)\varphi_n(s), \tag{28}$$

in terms of the eigenfunctions φ_n of the equation

$$\epsilon k_B T \frac{d^4}{ds^4}\varphi_n(s) - 2\nu k_B T \frac{d^2}{ds^2}\varphi_n(s) = \xi_n \varphi_n(s), \tag{29}$$

with the eigenvalues ($n \in \mathbb{N}_0$)

$$\xi_n = k_B T\left(\epsilon \zeta_n^4 + 2\nu \zeta_n^2\right). \tag{30}$$

The wave numbers ζ_n follow from the boundary conditions. For a passive flexible polymer, $pL \gg 1$, the wave numbers are $\zeta_n = n\pi/L$ and the eigenvalues $\xi_n = 2\nu k_B T \pi^2 n^2/L^2$. The stiffness dependence of ζ_n and ξ_n of passive semiflexible polymers is discussed in Ref. [96] and that for free draining active polymers in Ref. [44].

Insertion of the expansion (28) into Eq. (21) yields the equation

$$\frac{d\boldsymbol{\chi}_n(t)}{dt} = \sum_{m=0}^{\infty} H_{nm}[3\pi\eta \boldsymbol{v}_m(t) + \boldsymbol{\Gamma}_m(t) - \xi_m \boldsymbol{\chi}_m(t)] \tag{31}$$

for the mode amplitudes $\boldsymbol{\chi}_n$, where $H_{nm} = (\delta_{nm} + 3\pi\eta\Omega_{nm})/3\pi\eta$ is the hydrodynamic tensor in mode representation [84]. The second moments of the stochastic-force amplitudes $\boldsymbol{\Gamma}_n(t)$ are given by

$$\langle \Gamma_{n\alpha}(t)\, \Gamma_{m\beta}(t')\rangle = 2k_B T \delta_{\alpha\beta}\delta(t-t')\, H^{-1}_{nm}. \tag{32}$$

The mode representation of the correlation function (25) of the active velocity is [42]

$$\langle \boldsymbol{v}_n(t)\cdot \boldsymbol{v}_m(t')\rangle = v_0^2 l e^{-\gamma_R|t-t'|}\delta_{nm}. \tag{33}$$

In Eq. (31) all modes couple in general and the set of equations can only be solved numerically. To arrive at an analytical solution, we neglect the off-diagonal terms of the hydrodynamic-mode tensor H_{nm}, which yields [84,86,95] ($n > 0$)

$$\frac{d\boldsymbol{\chi}_n(t)}{dt} = -\frac{1}{\tilde{\tau}_n}\boldsymbol{\chi}_n + H_{nn}[\boldsymbol{\Gamma}_n(t) + 3\pi\eta \boldsymbol{v}_n(t)], \tag{34}$$

with the relaxation times

$$\tilde{\tau}_n = \frac{1}{H_{nn}\xi_n} = \frac{\tau_n}{1+3\pi\eta\Omega_{nn}}, \tag{35}$$

and $\tau_n = 3\pi\eta/\xi_n$ the relaxation times in the absence of hydrodynamic interactions. For passive flexible polymers [44,96]

$$\tau_n = \frac{3\eta L^2}{2\nu k_B T \pi n^2}. \tag{36}$$

The stationary-state solution of Eq. (34) for $n > 0$ is

$$\boldsymbol{\chi}_n(t) = H_{nn}\int_{-\infty}^{t} dt'\, e^{-(t-t')/\tilde{\tau}_n}[3\pi\eta \boldsymbol{v}_n(t') + \boldsymbol{\Gamma}_n(t')], \tag{37}$$

and for $n = 0$

$$\boldsymbol{\chi}_0(t) = \boldsymbol{\chi}_0(0) + \int_0^t dt'\, H_{00}[3\pi\eta \boldsymbol{v}_{(0)}(t') + \boldsymbol{\Gamma}_0(t')]. \tag{38}$$

3. Correlation functions

The correlation functions of the mode amplitudes are given by ($n > 0$)

$$\langle \boldsymbol{\chi}_n(t)\cdot\boldsymbol{\chi}_m(t')\rangle = \delta_{nm}\left[\frac{k_B T\tau_n}{\pi\eta}e^{-|t-t'|/\tilde{\tau}_n} + \frac{v_0^2 l\tau_n^2}{1-(\gamma_R\tilde{\tau}_n)^2} \times (e^{-\gamma_R|t-t'|} - \gamma_R\tilde{\tau}_n e^{-|t-t'|/\tilde{\tau}_n})\right], \tag{39}$$

and for $n = 0$

$$\langle \boldsymbol{\chi}_0(t)\cdot\boldsymbol{\chi}_0(t')\rangle = \langle \boldsymbol{\chi}_0^2(0)\rangle + 6k_B T\, H_{00}\, t' + (3\pi\eta H_{00})^2\frac{v_0^2 l}{\gamma_R^2}(2\gamma_R t' - 1 - e^{\gamma_R(t'-t)} + e^{-\gamma_R t} + e^{-\gamma_R t'}). \tag{40}$$

Inserting the eigenfunction expansion (28) into the mean-square distance $a^2(s,s')$, we obtain

$$a^2(s,s') = \sum_{n=1}^{\infty}\langle \boldsymbol{\chi}_n^2\rangle[\varphi_n(s) - \varphi_n(s')]^2, \tag{41}$$

with the stationary-state correlation functions (39)

$$\langle \boldsymbol{\chi}_n^2\rangle = \frac{k_B T\tau_n}{\pi\eta} + \frac{v_0^2 l\tau_n^2}{1+\gamma_R\tilde{\tau}_n}, \tag{42}$$

which depend on the hydrodynamic interactions via $\tilde{\tau}_n$. The active term with v_0^2 leads to enhanced fluctuations, which are most significant at small mode numbers [51], and reflects the violation of the fluctuation-dissipation relation [100]. Notably, hydrodynamic interactions affect the dynamics as well as the stationary-state conformational properties of an active polymer, in contrast to passive systems, where conformational properties are independent of HIs.

4. Mean square distance and hydrodynamic tensor: Mode representation

The exact analytical expression of the mean-square distance $a^2(s,s')$ (41) for the flexible active polymer can be calculated by (numerically) performing the sum in Eq. (41), where, in general, $a^2(s,s')$ depends on s and s'. However, the relaxation times $\tilde{\tau}_n$ are required, which depend via $a^2(s,s')$ on the Oseen tensor. Hence, the double integral

$$\Omega_{nn} = \sqrt{\frac{1}{6\pi^3\eta^2}}\int_{-L/2}^{L/2}\int_{-L/2}^{L/2}\Theta(|s-s'|-d_H) \times \frac{\varphi_n(s)\varphi_n(s')}{\sqrt{a^2(s,s')}}\, ds'\, ds \tag{43}$$

has to be evaluated together with Eq. (41) in an iterative and self-consistent manner, which constitutes a major computational challenge.

For a passive semiflexible polymer, $a^2(s,s')$ is only a function of the difference $|s-s'|$ [83,84]. In order to find a more easily tractable expression for an active polymer, we replace the difference of the eigenfunctions in Eq. (41) by the expression valid for a passive polymer, namely, $\varphi_n(s) - \varphi_n(s') = 2\sin[n\pi(s-s')/2L]$ for n odd and $\varphi_n(s) - \varphi_n(s') =$

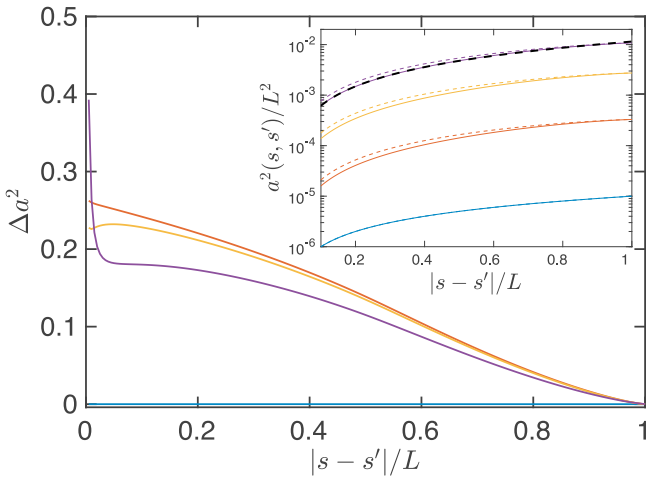

FIG. 6. Ratio $\Delta a^2 = |a^2(s,s') - a^2(s-s')|/a^2(s,s')$ of the difference between the mean-square distance between two points along the polymer contour, Eq. (41), and its approximation, Eq. (44), and Eq. (41) for $pL = 10^3$ and the Péclet numbers $\mathrm{Pe} = 10^{-2}$ (blue, bottom), 1 (orange), 50 (yellow), and 10^3 (purple) (top to bottom at 0.2). Inset: Mean-square distance between two points along the polymer contour. The solid lines are obtained from Eq. (41), where $s' = -L/2$, and the dashed lines from the approximation (44). The long-dashed line for $\mathrm{Pe} = 10^3$ is a power-law fit, which yields $a^2(s) = 0.11 s^{1.27}$. Colors correspond to the same Péclet numbers as in the main plot and increase from bottom to top.

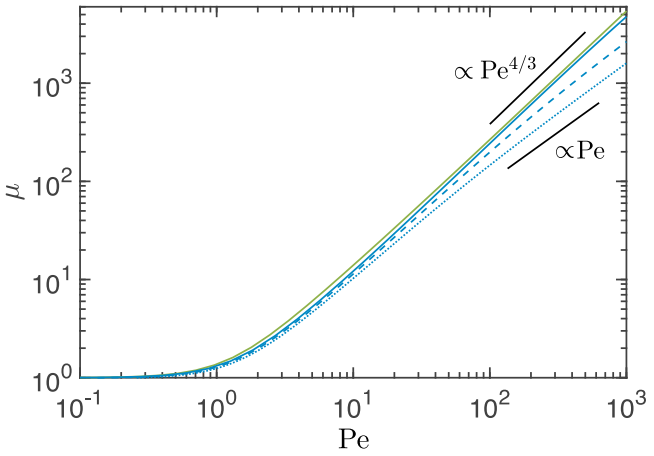

FIG. 7. Normalized stretching coefficient $\mu = 2\nu/(3p)$, solution of Eq. (46), as function of the Péclet number Pe for flexible polymers with $pL = 50$ (dotted), 1.5×10^2 (dashed), and 10^3 (solid blue, bottom). The top solid line (green) shows the result of an active polymer in the absence of HIs for $pL = 10^3$. The short lines (black) indicate the power-law dependence in the respective regimes.

0 for n even. As a result, we obtain the expression

$$a^2(s) = \frac{8}{L} \sum_{n,\mathrm{odd}} \left(\frac{k_B T \tau_n}{\pi \eta} + \frac{v_0^2 l \tau_n^2}{1 + \gamma_R \tilde{\tau}_n} \right) \sin^2 \left(\frac{n\pi}{2L} s \right). \quad (44)$$

This leads to the more easily tractable expression for the Oseen tensor (43) with a single integral

$$\Omega_{nn} = \sqrt{\frac{2}{3\pi^3}} \frac{1}{\eta L} \int_{d_H}^{L} \frac{L-s}{\sqrt{a^2(s)}} \cos \left(\frac{n\pi}{L} s \right) ds \quad (45)$$

by applying a standard approximation for the double integral, which is dominated by contributions with $s = s'$ (cf. Ref. [86]). This expression is identical with that of a passive polymer aside from the distance $a^2(s-s')$, which depends here on activity via the relaxation times [84]. As shown in Fig. 6, the approximations employed in deriving Eq. (44) capture the dependence of $a^2(s,s')$ on the contour coordinate well, the better the larger the Péclet number.

In the following, when not indicated otherwise, the approximate expressions (44) and (45) are used for the calculation of the Oseen tensor. Moreover, we use $\Delta = 0.6$ [cf. Eq. (11) for the definition of Δ].

5. Stretching coefficient and relaxation times

For flexible polymers with $L/l = pL \gg 1$, the constraint (22) for the stretching coefficient $\mu = 2\nu/(3p)$ turns into

$$\sum_{n=1}^{\infty} \left[\frac{k_B T \tau_n}{\pi \eta} + \frac{v_0^2 l \tau_n^2}{1 + \gamma_R \tilde{\tau}_n} \right] \zeta_n^2 = L, \quad (46)$$

with the eigenfunction expansion (28) and the relaxation times [Eq. (35)]

$$\tilde{\tau}_n = \frac{\tau_R}{\mu n^2 (1 + 3\pi \eta \Omega_{nn})}, \quad (47)$$

where $\tau_R = \eta L^2/(\pi k_B T p)$ is the Rouse relaxation time [86,96]. Due to nonlinear terms, specifically in Ω_{nn}, the related equations and expressions have to be solved and evaluated numerically.

The scaled stretching coefficient, $\mu = 2\nu/(3p)$, is presented in Fig. 7 as a function of the Péclet number. For short polymers or large stiffness ($pL = 50$), μ increases linearly with increasing Pe in the limit $1 \ll pL \ll \mathrm{Pe}$ [cf. Eq. (A2)]. In case of more flexible polymers ($pL \gtrsim 10^3$), $\mu \sim \mathrm{Pe}^{4/3}$ in the range $1 \ll \mathrm{Pe} \ll pL$ [cf. Eq. (A3)]. The overall dependence of μ on Pe resembles that of a polymer in the absence of hydrodynamic interactions [42]. Yet hydrodynamics affects μ, particularly for Péclet numbers in the vicinity of $\mathrm{Pe} \approx 10$. In the Appendix, a more detailed discussion of the asymptotic dependencies is provided.

Figure 8(a) depicts the dependence of the preaveraged Oseen tensor on the mode number for flexible polymers. For a passive polymer, we obtained the dependence $\Omega_{nn} \sim n^{-1/2}$ of the Zimm model [86] over a range of mode numbers, which depends on pL. With increasing Péclet number, both the values of Ω_{nn} and the magnitude of the slope decrease substantially. As a consequence, at high Péclet numbers, Ω_{nn} does not contribute to the mode-number dependence of the relaxation time anymore, as is reflected in Fig. 8(b). Zimm-type relaxation times $\tilde{\tau}_n \sim n^{-3/2}$ are obtained for the passive polymer [Fig. 8(b)] [84]. With increasing Péclet number, the mode-number dependence changes to $\tilde{\tau}_n \sim n^{-7/4}$ for $\mathrm{Pe} = 10^3$, a dependence very close to that of a free-draining, nonhydrodynamic Rouse polymer [86]. This emphasizes the diminishing effect of hydrodynamic interactions with increasing activity.

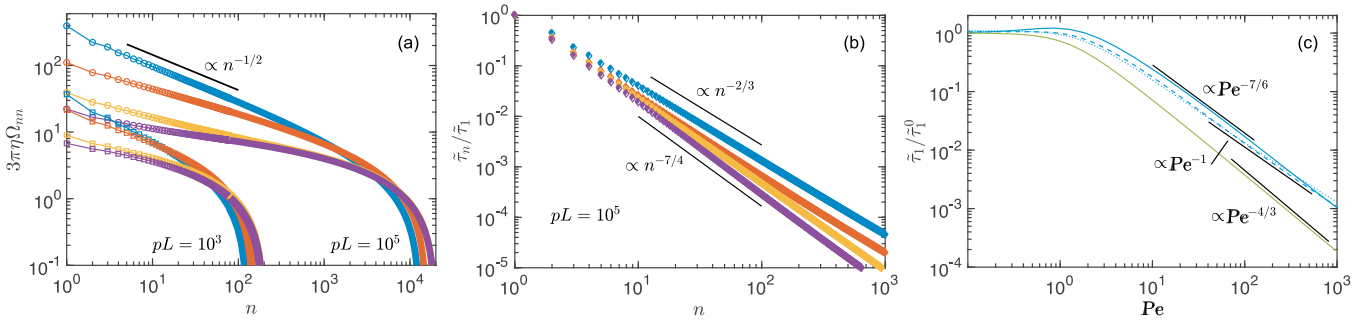

FIG. 8. (a) Mode-number dependence of the Oseen tensor Ω_{nn} for polymers of length $pL = 10^3$ (squares) and $pL = 10^5$ (circles) and the Péclet numbers $\mathrm{Pe} = 10^{-2}$ (blue), 1 (orange), 50 (yellow), and 10^3 (purple) (top to bottom). (b) Mode-number dependence of the relaxation times $\tilde{\tau}_n$ for flexible polymers of length $pL = 10^5$ and the Péclet numbers $\mathrm{Pe} = 0$ (blue), 1 (orange), 50 (yellow), and 10^3 (purple) (top to bottom). (c) Longest polymer relaxation time $\tilde{\tau}_1$, Eq. (47), normalized by the corresponding passive value $\tilde{\tau}_1^0$ as function of the Péclet number Pe for flexible polymers with $pL = 50$ (dotted), 1.5×10^2 (dashed), and 10^3 (solid blue, top). The bottom solid curve (green) corresponds to an active polymer in the absence of HIs for $pL = 10^3$, where $\tau_1 \sim \mathrm{Pe}^{-4/3}$. The short lines (black) indicate power-law dependencies in the respective regimes.

The activity dependence of the longest polymer relaxation time is displayed in Fig 8(c). The decline of $\tilde{\tau}_1$ with increasing Pe is determined by the stretching coefficient μ and the implicit dependence of Ω_{11} on $\mu(\mathrm{Pe})$. The shift to larger Pe of the curves in the presence of HIs reflects its influence on the relaxation times, specifically the influence on Ω_{11}. The latter is also responsible for values $\tilde{\tau}_1/\tilde{\tau}_1^0 > 1$ ($\mathrm{Pe} \approx 1$), because Ω_{11} decreases with increasing Pe [Fig. 8(a)]. As discussed in the Appendix, μ is essentially independent of hydrodynamic interactions for $pL \ll \mathrm{Pe}$, hence the decline of $\tilde{\tau}_1$ with increasing Pe ($\mathrm{Pe} \gg 1$) for $pL = 50$ is solely determined by μ and $\tilde{\tau}_1 \sim 1/\mathrm{Pe}$. Similarly, the asymptotic behavior for $pL = 10^3$ is determined by μ, with $\tilde{\tau}_1 \sim 1/\mathrm{Pe}^{4/3}$, the dependence of a polymer in the absence of hydrodynamic interactions. However, for very flexible polymers, $pL \gtrsim 10^3$, the HIs give rise to an intermediate regime, $10 < \mathrm{Pe} < 10^3$, where $\tilde{\tau}_1 \sim \mathrm{Pe}^{-7/6}$. The difference to a decay with $\tilde{\tau}_1 \sim \mathrm{Pe}^{-1}$ seems subtle, but is essential and strongly affects the conformational and dynamical properties of a polymer, as will be discussed in Secs. V and VI.

V. CONFORMATIONAL PROPERTIES

The conformational properties of the polymers are characterized by their mean-square end-to-end distance $\langle \boldsymbol{r}_e^2 \rangle = \langle (\boldsymbol{r}(L/2) - \boldsymbol{r}(-L/2))^2 \rangle$, which is

$$\langle \boldsymbol{r}_e^2 \rangle = \frac{8}{L} \sum_{n,\,\mathrm{odd}} \left(\frac{k_B T \tau_n}{\pi \eta} + \frac{v_0^2 l \tau_n^2}{1 + \gamma_R \tilde{\tau}_n} \right) \tag{48}$$

in terms of the mode amplitudes of Eq. (42). Numerical results for $\langle \boldsymbol{r}_e^2 \rangle$ are displayed in Fig. 9. As in simulations (cf. Fig. 2), polymers swell stronger with increasing activity than free draining active polymers, and their size saturates at $L^2/2$ for $\mathrm{Pe} \to \infty$, the value of the free-draining case. Similarly to free-draining polymers or polymers with self-propelled monomers, the thermal contribution, proportional to $k_B T$, decreases and the active term, proportional to v_0^2, increases with increasing Pe. However, the swelling behavior is distinctly different compared to those two cases, which is reflected by the respective dependence on the relaxation times τ_n and $\tilde{\tau}_n$. Comparing the relaxation-time dependence of the active term (with v_0) of a free-draining polymer, $\tau_n^2/(1 + \gamma_R \tau_n)$ [42], of a polymer with self-propelled monomers, $\tilde{\tau}_n^2/(1 + \gamma_R \tilde{\tau}_n)$ [78], and that of Eq. (48), we find

$$\frac{\tau_n^2}{1 + \gamma_R \tilde{\tau}_n} \geqslant \frac{\tau_n^2}{1 + \gamma_R \tau_n} \geqslant \frac{\tilde{\tau}_n^2}{1 + \gamma_R \tilde{\tau}_n}, \tag{49}$$

because $\tilde{\tau}_n \leqslant \tau_n$. Hence, the externally driven polymer swells strongest with increasing Péclet number, and swelling sets in at smaller Pe. This is reflected in the shift of the dashed-dotted lines in Fig. 9 to smaller Pe with increasing pL, whereas respective curves shift to larger Pe in case of polymers with self-propelled monomers, associated with polymer shrinkage [78]. This reveals the distinct influence of the character of the

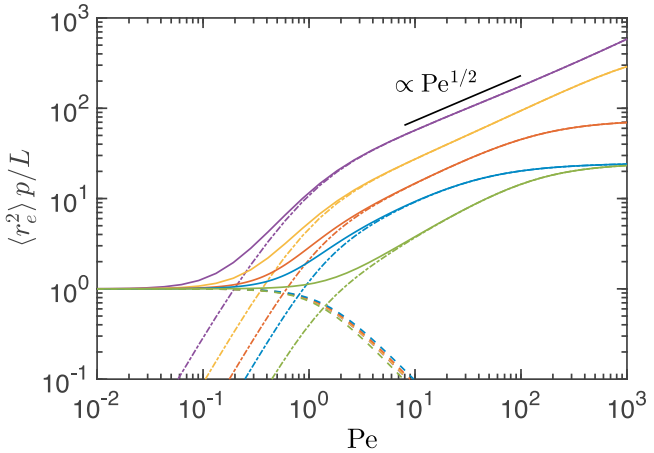

FIG. 9. Polymer mean-square end-to-end distance $\langle \boldsymbol{r}_e^2 \rangle$ scaled by the equilibrium value L/p in the presence of HIs as a function of the Péclet number Pe for flexible polymers of length $pL = 50$ (blue), $pL = 1.5 \times 10^2$ (orange), $pL = 10^3$ (yellow), and $pL = 10^4$ (purple) (pL increases from top to bottom). The green curve (bottom) corresponds to the free-draining flexible polymer with $pL = 50$. The dashed curves represent the passive contribution with the relaxation times τ_n and the dashed-dotted curves the active part with v_0^2 in Eq. (48). The short line (black) indicates a power-law dependence in the respective regime.

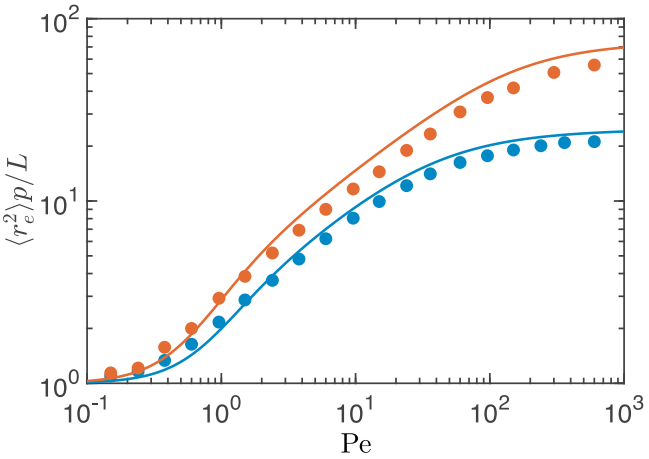

FIG. 10. Comparison of the dependence of the polymer mean-square end-to-end-distance on the Péclet number obtained from analytical theory (lines) and BD simulations (bullets) for polymers with $pL = 50$ (blue, bottom) and $pL = 1.5 \times 10^2$ (orange, top).

active noise on the polymer conformations in the presence of hydrodynamic interactions.

The asymptotic limit for $\mathrm{Pe} \to \infty$ can be obtained analytically. The term $\gamma_R \tilde{\tau}_n \ll 1$ for $\mathrm{Pe} \to \infty$ (cf. the Appendix) and, thus, can be neglected in Eq. (48). Evaluation of the sum over modes with the relaxation times (36) and insertion of Eq. (A2) then gives $\langle \boldsymbol{r}_e^2 \rangle = L^2/2$. This result is in close agreement with simulations, which yield a somewhat smaller value, as shown in Fig. 10. Moreover, the asymptotic limit is identical with that of a free-draining polymer [42], in contrast to a polymer of self-propelled monomers [78].

The enhanced swelling of the externally driven flexible polymer can be understood as follows. In the regime of strong polymer swelling, e.g., $0.1 < \mathrm{Pe} < 100$ for $pL = 50$ in Fig. 9, $\gamma_R \tilde{\tau}_1 \gg 1$ and the active velocity-dependent term in Eq. (42) can be approximate by

$$\frac{v_0^2 l \tau_n}{\gamma_R}(1 + 3\pi\eta\Omega_{nn}), \tag{50}$$

which is by the contribution $3\pi\eta\Omega_{nn}$ larger than the term in the absence of HIs. Formally, we can introduce an effective larger velocity $v_0\sqrt{1 + 3\pi\eta\Omega_{nn}}$, which corresponds to an effectively higher Péclet number and, hence, a stronger polymer swelling. According to Eq. (37), both the active velocity $\boldsymbol{v}_n(t)$ and the stochastic force $\boldsymbol{\Gamma}_n(t)$ are enhanced by the hydrodynamic tensor H_{nn}. However, the hydrodynamic effect disappears in the thermal contribution of the correlation function (42), because of the fluctuation-dissipation relation Eq. (32). Hence, the strong hydrodynamic effect on polymer conformations is a consequence of the independence of the rotational dynamics from the translational hydrodynamic tensor [cf. Eq. (33)].

Simulations (Fig. 2) and analytical calculations (Fig. 9) predict the swelling behavior $\langle \boldsymbol{r}_e^2 \rangle \sim \mathrm{Pe}^{1/2}$ over a range of Péclet numbers, where the range increases with increasing pL. This dependence on Pe is markedly different from that of free-draining polymers and those with self-propelled monomers; in the latter case the exponent is larger than unity [78]. This difference rests upon a particular dependence of the dynamics on hydrodynamic interactions, reflected in the Pe dependence of the relaxation time $\tilde{\tau}_1$ [Fig. 8(c)], as can be shown analytically. First, the mode-number dependence of the relaxation times $\tilde{\tau}_n$ is well described by a power law, specifically for $pL = 10^3$, $\tilde{\tau}_n \approx \tilde{\tau}_1/n^2$ [Fig. 8(b)]. Second, in the relevant Pe regime $\gamma_R \tilde{\tau}_n \gg 1$, hence, Eq. (48) yields

$$\langle \boldsymbol{r}_e^2 \rangle \sim \frac{\mathrm{Pe}^2}{\mu^2 \tilde{\tau}_1} \sim \sqrt{\mathrm{Pe}}, \tag{51}$$

with $\mu \sim \mathrm{Pe}^{4/3}$ [Eq. (A3)] and $\tilde{\tau}_1 \sim \mathrm{Pe}^{-7/6}$ [Fig. 8(c)], relations appropriate for $pL = 10^3$. It is the Pe dependence of the relaxation time $\tilde{\tau}_1$ which is decisive for the relation (51). In the absence of HIs, $\tau \sim 1/\mu \sim \mathrm{Pe}^{-4/3}$ and $\langle \boldsymbol{r}_e^2 \rangle \sim \mathrm{Pe}^{2/3}$ [42], which is a substantially stronger Pe dependence. The seemingly rather small difference between the exponent $-4/3 = -8/6$, valid in the absence of HIs, and $-7/6$, valid with HIs, of the relaxation time is decisive and leads to a weaker swelling of the externally driven polymer with increasing Pe.

The theoretical approach very well reproduces the simulation data, as shown in Fig. 10. The analytical theory somewhat overestimates the asymptotic value as a consequence of the mean-field-type constraint for the bond length [Eq. (22)].

We like to emphasize that the swelling of active polymers is determined by their inextensibility, as is evident from the results of this section. Only by taking this polymer feature suitably into account, e.g., via the constraint (22), the qualitative correct behavior is obtained theoretically [42,44,46,51,78]. Approaches neglecting such a condition predict swelling, which qualitatively and quantitatively disagrees with simulation results.

VI. DYNAMICAL PROPERTIES

The polymer dynamics is analyzed in terms of the monomer mean-square displacement (MSD) averaged over the polymer contour

$$\begin{aligned}\overline{\langle \Delta \boldsymbol{r}^2(t) \rangle} &= \frac{1}{L}\int ds \langle (\boldsymbol{r}(s,t) - \boldsymbol{r}(s,0))^2 \rangle \\ &= \langle \Delta \boldsymbol{r}_{cm}^2(t) \rangle + \langle \Delta \boldsymbol{r}_0^2(t) \rangle + \langle \Delta \boldsymbol{r}_a^2(t) \rangle,\end{aligned} \tag{52}$$

with the center-of-mass mean-square displacement

$$\begin{aligned}\langle \Delta \boldsymbol{r}_{cm}^2(t) \rangle = {} & H_{00}\frac{6k_BT}{L}t \\ & + (1 + 3\pi\eta\Omega_{00})\frac{2v_0^2 l}{\gamma_R^2 L}(\gamma_R t - 1 + e^{-\gamma_R t}),\end{aligned} \tag{53}$$

$H_{00} = (1 + 3\pi\eta\Omega_{00})/(3\pi\eta)$, the activity-modified equilibrium-like internal dynamics contribution

$$\langle \Delta \boldsymbol{r}_0^2(t) \rangle = \frac{1}{L}\sum_{n=1}^{\infty}\frac{2k_BT\tau_n}{\pi\eta}(1 - e^{-t/\tilde{\tau}_n}), \tag{54}$$

and the active contribution

$$\langle \Delta \boldsymbol{r}_a^2(t) \rangle = \frac{1}{L}\sum_{n=1}^{\infty}\frac{2v_0^2 l \tau_n^2}{1 + \gamma_R\tilde{\tau}_n}\left(1 - \frac{e^{-\gamma_R t} - \gamma_R\tilde{\tau}_n e^{-t/\tilde{\tau}_n}}{1 - \gamma_R\tilde{\tau}_n}\right). \tag{55}$$

The passive parts of $\overline{\langle \Delta \boldsymbol{r}^2(t) \rangle}$—in $\langle \Delta \boldsymbol{r}_{cm}^2(t) \rangle$ and $\langle \Delta \boldsymbol{r}_0^2(t) \rangle$—are, aside from the μ dependence of the relaxation

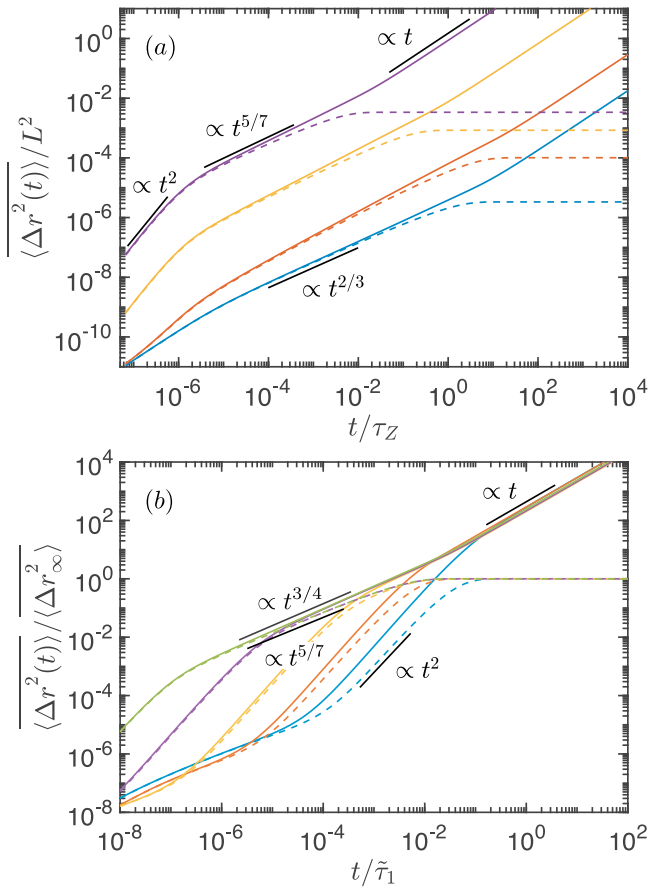

FIG. 11. (a) Mean-square displacement of flexible polymers for $pL = 10^5$ and the Péclet numbers Pe = 0 (blue), 1 (orange), 50 (yellow), and 10^3 (purple) (bottom to top). The Zimm relaxation time $\tau_Z = \eta(L/p)^{3/2}/(\sqrt{3\pi}k_BT)$ is the longest relaxation time of the passive polymer. (b) MSD for the Péclet number Pe = 115 and $pL = 50$ (blue), 1.5×10^2 (orange), 10^3 (yellow), 10^4 (purple), and 10^5 (green) (bottom to top). The dashed lines correspond to the MSD in the polymer center-of-mass reference frame, and the solid lines are the overall MSD. The short lines (black) indicate power laws in the respective regimes.

times, identical with the dynamics of the Zimm model, or that of a semiflexible polymer in the presence of HIs [78,86,95]. Numerical results for Eq. (52) are presented in Fig. 11.

The center-of-mass MSD exhibits the same time-dependent terms as an active polymer without HIs and a polymer with self-propelled monomers. For $t \to \infty$, $\langle \Delta \boldsymbol{r}^2_{cm}(t)\rangle$ dominates the total MSD, increasing linearly in time with the diffusion coefficient

$$D = \frac{1 + 3\pi\eta\Omega_{00}}{L}\left(\frac{k_BT}{3\pi\eta} + \frac{v_0^2 l}{3\gamma_R}\right), \tag{56}$$

which is the diffusion coefficient in the absence of HIs, the term in brackets, modified by hydrodynamics, Ω_{00}; the latter depends on polymer length and Péclet number. Figure 8(a) indicates a substantial increase of Ω_{00} with polymer length, a decrease with increasing Pe, and Ω_{00} seems to approach a Pe-independent value for Pe $\gg 1$.

The site-averaged MSD in the center-of-mass reference frame, $\langle \Delta \boldsymbol{r}^2_0(t)\rangle + \langle \Delta \boldsymbol{r}^2_a(t)\rangle$, exhibits three distinct regimes:

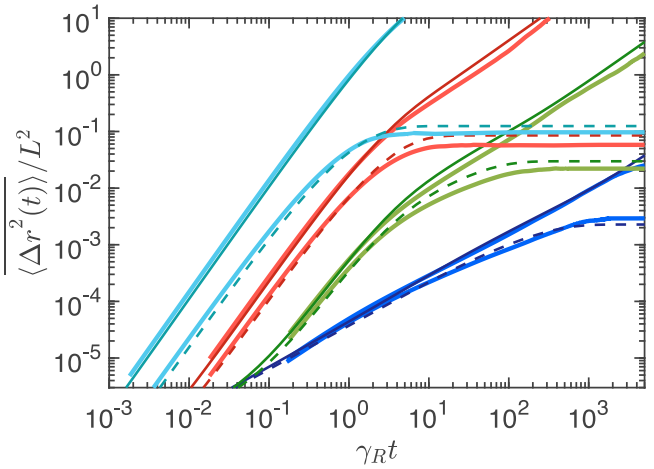

FIG. 12. Comparison of the mean-square displacement obtained in simulations (broad solid lines; Fig. 5) with analytical theory [thin solid and dashed lines; Eq. (52)] for the Péclet numbers Pe = 0 (blue), 10^1 (green), 10^2 (red), and 10^3 (cyan) (bottom to top). The monomer number is $N_m = 150$ and $pL = L/l = 150$, respectively. The dashed lines and the respective broad solid lines correspond to the MSD in the polymer center-of-mass reference frame.

(i) $t \to 0$—The MSD is dominated by Eq. (54), and all modes contribute. With $\tau_n = \tau_R/(\mu n^2)$ for a flexible polymer, conversion of the sum to an integral yields

$$\langle \Delta \boldsymbol{r}^2_0(t)\rangle = \frac{2L}{\pi^2 p\mu}\left(\frac{t}{\tilde{\tau}_1}\right)^{2/3}\int_0^\infty dx \frac{1 - e^{-x^{3/2}}}{x^2}. \tag{57}$$

This is the same relation as obtained for a passive system, except that μ and $\tilde{\tau}_1$ depend on activity, and a polymer with self-propelled monomers [78].

(ii) $t/\tilde{\tau}_1$ and $\gamma_R t \ll 1$—Taylor expansion of the exponential functions in Eq. (55) yields

$$\langle \Delta \boldsymbol{r}^2_a(t)\rangle = \frac{v_0^2 l \gamma_R}{L}\sum_{n=1}^{\infty}\frac{\tau_n^2}{\tilde{\tau}_n(1 + \gamma_R\tilde{\tau}_n)}t^2, \tag{58}$$

consistent with the observed ballistic regime in Fig. 11. This regime and its dependence on activity and polymer properties is in qualitative agreement with the simulation results of Fig. 5 (cf. Fig. 12).

(iii) $1/\gamma_R \ll t \ll \tilde{\tau}_1$—With $\gamma_R\tilde{\tau}_1 \gg 1$, the MSD is given by

$$\langle \Delta \boldsymbol{r}^2_a(t)\rangle = \frac{2v_0^2 l}{\gamma_R L}\sum_{n=1}^{\infty}\frac{\tau_n^2}{\tilde{\tau}_n}\left(1 - e^{-t/\tilde{\tau}_n}\right). \tag{59}$$

The relaxation times $\tilde{\tau}_n$ are well described by the power law $\tilde{\tau}_n = \tilde{\tau}_1/n^\gamma$ (cf. Fig. 8). Inserting this relation and replacing the sum by an integral, Eq. (59) yields

$$\langle \Delta \boldsymbol{r}^2_a(t)\rangle = \frac{2v_0^2 l\tau_R^2}{\mu^2\gamma_R L}\left(\frac{t}{\tilde{\tau}_1}\right)^{\gamma'}\int_0^\infty dx\, \frac{1 - e^{-x^\gamma}}{x^{4-\gamma}}, \tag{60}$$

with $\gamma' = 3/\gamma - 1$. For Pe > 50 and $pL = 10^3$, the power-law exponent is close to $\gamma = 7/4$, hence,

$$\langle \Delta \boldsymbol{r}^2_a(t)\rangle \sim t^{5/7}. \tag{61}$$

This time dependence is in close agreement with the numerical result displayed in Fig. 11. By the interplay between activity and hydrodynamic interactions, a new power-law regime emerges for the intramolecular MSD. The seemingly small difference between the exponent of the relaxation times $\gamma = 7/4$ and the value $\gamma = 2$ for Rouse polymers, implies a significantly different power law of the MSD, namely an exponent $\gamma' = 5/7$ for the current active polymers versus $\gamma' = 1/2$ for Rouse polymers [44]. Moreover, the type of active force matters—calculations for self-propelled monomers yield the exponent $\gamma' = 2/5$ [78], which is even smaller than the value for free-draining polymers. This emphasizes the strong and dominating influence of hydrodynamic interactions on the dynamics of active polymers.

The overall monomer MSD (52) exhibits even a different power-law regime $\langle \Delta \boldsymbol{r}^2(t) \rangle \sim t^{3/4}$ for $pL \gtrsim 10^3$, by an additional contribution of the center-of-mass MSD. Evidently, a splitting of the center-of-mass-site MSD, $\langle \Delta \boldsymbol{r}_0^2(t) \rangle + \langle \Delta \boldsymbol{r}_a^2(t) \rangle$, from the overall MSD is not possible, even for very long polymers.

Figure 12 presents a comparison of the mean-square displacements of the discrete polymers of Fig. 5 with analytically results. The results agree very well considering the limited statistical accuracy in the simulation results, the approximation in the analytical evaluation of the hydrodynamic tensor, and the overestimation of the extension of active polymers for $\mathrm{Pe} \gg 1$ (cf. Fig. 10) as a consequence of the mean-field-type constraint for the bond length. The latter is reflected by the analytical results exceeding the asymptotic values of the MSD in the polymer center-of-mass reference frame for $t \to \infty$, which is theoretically twice the radius of gyration, but somewhat smaller in simulations.

VII. SUMMARY AND CONCLUSIONS

We have studied the conformational and dynamical properties of semiflexible active polymers in the presence of hydrodynamic interactions by simulations and analytical theory. In the simulations, we consider the overdamped dynamics of a bead-spring polymer, including hydrodynamic interactions via the Rotne-Prager-Yamakawa hydrodynamic tensor. Moreover, we present an implementation of the active polymer in the multiparticle-collision-dynamics approach. Comparison of the polymer conformational properties at various Péclet numbers and polymer stiffness yields quantitative agreement between simulations employing the hydrodynamic tensor and the MPC method, respectively. The MPC approach opens possibilities to study active polymers in situations, where a tensor description is extremely difficult and demanding, as for polymers confined in channels. In the analytical treatment, the Gaussian semiflexible polymer model is adopted, taking into account the polymer inextensibility in a mean-field manner by a constraint for the average contour length. Here hydrodynamic interactions are taken into account by the preaveraged Oseen tensor. In any case, activity is modeled as a Gaussian colored-noise process with an exponential temporal correlation. This activity is assumed to be imposed externally onto the monomers by the embedding active bath. As a consequence, the active forces give rise to monomer Stokeslet flow fields, in contrast to self-propelled monomers which are force free [78]. Further Stokeslets appear by intramolecular forces due to bond, bending, volume exclusion, and thermal forces.

Our studies reveal a strong effect of hydrodynamics on both conformations and dynamics. As a consequence of the activity-induced Stokeslets, polymers swell monotonically and stronger with increasing Péclet number than active polymers in the absence of hydrodynamic interactions [42], and than polymers composed of self-propelled monomers [78]. In the asymptotic limit of an infinite Péclet number, the same finite mean-square end-to-end distance is assumed as for free-draining active polymers, larger than that of polymers with self-propelled monomers. As we have shown by analytical calculations, in this limit hydrodynamic interactions become irrelevant. Moreover, we find a broad range of Péclet numbers and stiffnesses, where the mean-square end-to-end distance increases as $\mathrm{Pe}^{1/2}$. This increase is slower compared to that of the other two types of active polymers. Here, the dependence of the longest relaxation time on the Péclet number plays a decisive role, with $\tilde{\tau}_1$ being strongly affected by hydrodynamic interactions.

Qualitatively, we explain the enhanced polymer swelling with increasing Pe by a hydrodynamically accelerated active velocity. In turn, this implies an apparent higher Péclet number, followed by stronger swelling. The flow field induced by translating parts of the polymers advects monomers or sites and leads to an accelerated dynamics. Similarly, an enhanced thermal force appears in the solution of the normal-mode amplitudes, $\boldsymbol{\chi}_n$, however, this effect is compensated by the fluctuation-dissipation relation. This implies that the thermal parts of conformational quantities at equilibrium are explicitly independent of hydrodynamic interactions. This does not apply to the active velocity, because its temporal correlation function is independent of hydrodynamics.

The polymer dynamics is determined by two relaxation processes, the orientational relaxation of an active site or monomer, and the polymer internal relaxation modes. This is reflected in distinct time regimes in the polymer mean-square displacement. At short times $t/\tilde{\tau}_1 \ll 1$ and $\gamma_R t \ll 1$, activity implies to a ballistic regime, with an enhanced dynamics compared to a passive polymer. For $1/\gamma_R \ll t \ll \tilde{\tau}_1$, the MSD is dominated by the internal dynamics, and a polymer-characteristic subdiffusive regime appears. Again, activity and hydrodynamics play a decisive role, leading to a power-law dependence of the site MSD in the polymer center-of-mass reference frame with an exponent $\gamma' = 5/7$, larger than that of a free-draining active polymer, and a polymer with self-propelled monomers and HIs. In the asymptotic limit of long times, the free-draining active diffusion coefficient is amplified by hydrodynamics, in the same way as the thermal diffusion coefficient [cf. Eq. (56)].

The analytical calculations and the good agreement with simulations indicate that a suitable account of the fixed polymer contour length is essential for a qualitative correct description of the active-polymer conformations. In the analytical calculations, we have been taking this constraint into account in a mean-field manner by the average mean-square contour length [Eq. (22)]. This leads to a strong activity dependence of the relaxation times and consequently the

observed increase of the mean-square end-to-end distance, $\langle \boldsymbol{r}_e^2 \rangle \sim \mathrm{Pe}^{1/2}$, and a saturation of $\langle \boldsymbol{r}_e^2 \rangle$ for $\mathrm{Pe} \to \infty$. Omission of this polymer property, as common in the theoretical description of active polymers by the Rouse or Zimm model, leads to artifacts especially at moderate and large activities.

In conclusion, in the presence of hydrodynamics, the properties of active polymers consisting either of self-propelled monomers or experiencing an external driving force with the same temporal correlation function are substantially different. In the first case, even flexible polymers shrink at moderate Péclet numbers and swell for larger Pe; in the second case, polymers swell monotonically for all Pe, and the polymer size is (significantly) larger for all Péclet numbers. The difference in the coupling to the fluid leads to a reduced or enhanced active velocity and is reflected in the polymer conformations and dynamics.

Experimentally, an externally driven polymer can in principle be realized by forcing a chain of colloidal particles by optical tweezers [101]. Optical forces are very well suited to manipulate objects as small as 5 nm and as large as hundreds of micrometers [101]. Combined with computer-generated holograms, many particles can be manipulated with a single laser beam at the same time. The example of an optical pump of Ref. [102] illustrates the possibility to manipulate several colloidal particle simultaneously. Such a setup is therefore well suited to actuated a colloidal polymer [48]. The persistent colloid motion can be controlled by the tweezer light field which translates them in random directions with an exponential temporal orientation correlation function.

ACKNOWLEDGMENTS

This research was funded by the European Union's Horizon 2020 research and innovation programme under Grant Agreement No. 674979-NANOTRANS. Financial support by the Deutsche Forschungsgemeinschaft (DFG) within the priority program SPP 1726 "Microswimmers-from Single Particle Motion to Collective Behaviour" is gratefully acknowledged. Moreover, the authors gratefully acknowledge the computing time granted through JARA-HPC on the supercomputer JURECA at Forschungszentrum Jülich.

APPENDIX: ASYMPTOTIC STRETCHING COEFFICIENT

The active contribution in the Eq. (46) can by written as

$$\sum_{i=1}^{\infty} \frac{v_0^2 l \tau_n^2}{1+\gamma_R \tilde{\tau}_n} \zeta_n^2 = \frac{\mathrm{Pe}^2 pL^2}{9\mu^2 \Delta^2 \pi^2} \times \sum_{i=1}^{\infty} \left[n^2 + \frac{2(pL)^2}{3\mu\Delta\pi^2(1+3\pi\eta\Omega_{nn})} \right]^{-1}, \tag{A1}$$

when we set $d_H \equiv l$. The stretching coefficient, μ, increases with increasing Pe. Hence, for $(pL)^2 \ll \mu$, the second term in the brackets can be neglected. Then we obtain from Eq. (46)

$$\mu = \sqrt{\frac{pL}{6}} \frac{\mathrm{Pe}}{3\Delta}. \tag{A2}$$

In the opposite limit, $pL \gg \mathrm{Pe}$, the sum over n is dominated by the second term in the bracket for small n, and the mode-number dependence is determined by the preaveraged Oseen tensor. With increasing Péclet number, higher modes become important, at the same time Ω_{nn} becomes less relevant. Neglecting the hydrodynamic contribution, or at least its mode-number dependence, the sum over modes can be evaluated, and Eq. (46) yields [42]

$$\mu \sim \mathrm{Pe}^{4/3}. \tag{A3}$$

[1] J. Elgeti, R. G. Winkler, and G. Gompper, Rep. Prog. Phys. **78**, 056601 (2015).
[2] M. C. Marchetti, J. F. Joanny, S. Ramaswamy, T. B. Liverpool, J. Prost, M. Rao, and R. A. Simha, Rev. Mod. Phys. **85**, 1143 (2013).
[3] M. E. Cates and J. Tailleur, Annu. Rev. Condens. Matter Phys. **6**, 219 (2015).
[4] C. Bechinger, R. Di Leonardo, H. Löwen, C. Reichhardt, G. Volpe, and G. Volpe, Rev. Mod. Phys. **88**, 045006 (2016).
[5] S. Ramaswamy, Nat. Phys. Rev. **1**, 640 (2019).
[6] G. Gompper, R. G. Winkler, T. Speck, A. Solon, C. Nardini, F. Peruani, H. Löwen, R. Golestanian, U. B. Kaupp, L. Alvarez *et al.*, J. Phys.: Condens. Matter **32**, 193001 (2020).
[7] M. R. Shaebani, A. Wysocki, R. G. Winkler, G. Gompper, and H. Rieger, Nat. Rev. Phys. **2**, 181 (2020).
[8] P. Romanczuk, M. Bär, W. Ebeling, B. Lindner, and L. Schimansky-Geier, Eur. Phys. J.: Spec. Top. **202**, 1 (2012).
[9] J. Bialké, T. Speck, and H. Löwen, Phys. Rev. Lett. **108**, 168301 (2012).
[10] G. S. Redner, M. F. Hagan, and A. Baskaran, Phys. Rev. Lett. **110**, 055701 (2013).
[11] Y. Fily, A. Baskaran, and M. F. Hagan, Soft Matter **10**, 5609 (2014).
[12] A. Wysocki, R. G. Winkler, and G. Gompper, Europhys. Lett. **105**, 48004 (2014).
[13] J. Stenhammar, D. Marenduzzo, R. J. Allen, and M. E. Cates, Soft Matter **10**, 1489 (2014).
[14] A. Wysocki, R. G. Winkler, and G. Gompper, New J. Phys. **18**, 123030 (2016).
[15] P. Digregorio, D. Levis, A. Suma, L. F. Cugliandolo, G. Gonnella, and I. Pagonabarraga, Phys. Rev. Lett. **121**, 098003 (2018).
[16] S. Das, G. Gompper, and R. G. Winkler, New J. Phys. **20**, 015001 (2018).
[17] J. Elgeti and G. Gompper, Europhys. Lett. **101**, 48003 (2013).
[18] S. C. Takatori, W. Yan, and J. F. Brady, Phys. Rev. Lett. **113**, 028103 (2014).
[19] A. P. Solon, J. Stenhammar, R. Wittkowski, M. Kardar, Y. Kafri, M. E. Cates, and J. Tailleur, Phys. Rev. Lett. **114**, 198301 (2015).
[20] R. G. Winkler, A. Wysocki, and G. Gompper, Soft Matter **11**, 6680 (2015).

[21] Y. Fily, Y. Kafri, A. P. Solon, J. Tailleur, and A. Turner, J. Phys. A: Math. Theor. **51**, 044003 (2018).
[22] S. Das, G. Gompper, and R. G. Winkler, Sci. Rep. **9**, 6608 (2019).
[23] S. Thakur and R. Kapral, Phys. Rev. E **85**, 026121 (2012).
[24] A. Suma, G. Gonnella, D. Marenduzzo, and E. Orlandini, Europhys. Lett. **108**, 56004 (2014).
[25] A. Furukawa, D. Marenduzzo, and M. E. Cates, Phys. Rev. E **90**, 022303 (2014).
[26] R. G. Winkler, Soft Matter **12**, 3737 (2016).
[27] J. T. Siebert, J. Letz, T. Speck, and P. Virnau, Soft Matter **13**, 1020 (2017).
[28] J. G. Gibbs, A. Nourhani, J. N. Johnson, and P. E. Lammert, MRS Adv. **2**, 3471 (2017).
[29] I. Petrelli, P. Digregorio, L. F. Cugliandolo, G. Gonnella, and A. Suma, Eur. Phys. J. E **41**, 128 (2018).
[30] D. Loi, S. Mossa, and L. F. Cugliandolo, Soft Matter **7**, 10193 (2011).
[31] A. Kaiser and H. Löwen, J. Chem. Phys. **141**, 044903 (2014).
[32] J. Harder, C. Valeriani, and A. Cacciuto, Phys. Rev. E **90**, 062312 (2014).
[33] A. Ghosh and N. S. Gov, Biophys. J. **107**, 1065 (2014).
[34] R. Chelakkot, A. Gopinath, L. Mahadevan, and M. F. Hagan, J. R. Soc., Interface **11**, 20130884 (2014).
[35] D. Sarkar, S. Thakur, Y.-G. Tao, and R. Kapral, Soft Matter **10**, 9577 (2014).
[36] H. Jiang and Z. Hou, Soft Matter **10**, 9248 (2014).
[37] A. Laskar and R. Adhikari, Soft Matter **11**, 9073 (2015).
[38] J. Shin, A. G. Cherstvy, W. K. Kim, and R. Metzler, New J. Phys. **17**, 113008 (2015).
[39] A. Kaiser, S. Babel, B. ten Hagen, C. von Ferber, and H. Löwen, J. Chem. Phys. **142**, 124905 (2015).
[40] R. E. Isele-Holder, J. Elgeti, and G. Gompper, Soft Matter **11**, 7181 (2015).
[41] N. Samanta and R. Chakrabarti, J. Phys. A: Math. Theor. **49**, 195601 (2016).
[42] T. Eisenstecken, G. Gompper, and R. G. Winkler, Polymers **8**, 304 (2016).
[43] J. Smrek and K. Kremer, Phys. Rev. Lett. **118**, 098002 (2017).
[44] T. Eisenstecken, G. Gompper, and R. G. Winkler, J. Chem. Phys. **146**, 154903 (2017).
[45] R. G. Winkler, J. Elgeti, and G. Gompper, J. Phys. Soc. Jpn. **86**, 101014 (2017).
[46] A. Martín-Gómez, G. Gompper, and R. G. Winkler, Polymers **10**, 837 (2018).
[47] V. Bianco, E. Locatelli, and P. Malgaretti, Phys. Rev. Lett. **121**, 217802 (2018).
[48] H. Löwen, Europhys. Lett. **121**, 58001 (2018).
[49] S. K. Anand and S. P. Singh, Phys. Rev. E **98**, 042501 (2018).
[50] N. Küchler, H. Löwen, and A. M. Menzel, Phys. Rev. E **93**, 022610 (2016).
[51] S. M. Mousavi, G. Gompper, and R. G. Winkler, J. Chem. Phys. **150**, 064913 (2019).
[52] M. E. Cates and F. C. MacKintosh, Soft Matter **7**, 3050 (2011).
[53] D. Needleman and Z. Dogic, Nat. Rev. Mater. **2**, 201748 (2017).
[54] A. J. Ridley, M. A. Schwartz, K. Burridge, R. A. Firtel, M. H. Ginsberg, G. Borisy, J. T. Parsons, and A. R. Horwitz, Science **302**, 1704 (2003).
[55] F. Jülicher, K. Kruse, J. Prost, and J.-F. Joanny, Phys. Rep. **449**, 3 (2007).
[56] J. Prost, F. Jülicher, and J.-F. Joanny, Nat. Phys. **11**, 111 (2015).
[57] A. Cordoba, J. D. Schieber, and T. Indei, RSC Adv. **4**, 17935 (2014).
[58] S. Ganguly, L. S. Williams, I. M. Palacios, and R. E. Goldstein, Proc. Natl. Acad. Sci. USA **109**, 15109 (2012).
[59] A. Ravichandran, G. A. Vliegenthart, G. Saggiorato, T. Auth, and G. Gompper, Biophys. J. **113**, 1121 (2017).
[60] Y. Harada, A. Noguchi, A. Kishino, and T. Yanagida, Nature (London) **326**, 805 (1987).
[61] F. J. Nédélec, T. Surrey, A. C. Maggs, and S. Leibler, Nature (London) **389**, 305 (1997).
[62] V. Schaller, C. Weber, C. Semmrich, E. Frey, and A. R. Bausch, Nature (London) **467**, 73 (2010).
[63] Y. Sumino, K. H. Nagai, Y. Shitaka, D. Tanaka, K. Yoshikawa, H. Chate, and K. Oiwa, Nature (London) **483**, 448 (2012).
[64] C. P. Brangwynne, G. H. Koenderink, F. C. MacKintosh, and D. A. Weitz, Phys. Rev. Lett. **100**, 118104 (2008).
[65] C. A. Weber, R. Suzuki, V. Schaller, I. S. Aranson, A. R. Bausch, and E. Frey, Proc. Natl. Acad. Sci. USA **112**, 10703 (2015).
[66] S. C. Weber, A. J. Spakowitz, and J. A. Theriot, Proc. Natl. Acad. Sci. USA **109**, 7338 (2012).
[67] A. Javer, Z. Long, E. Nugent, M. Grisi, K. Siriwatwetchakul, K. D. Dorfman, P. Cicuta, and M. Cosentino Lagomarsino, Nat. Commun. **4**, 3003 (2013).
[68] A. Zidovska, D. A. Weitz, and T. J. Mitchison, Proc. Natl. Acad. Sci. USA **110**, 15555 (2013).
[69] C. P. Brangwynne, G. H. Koenderink, F. C. MacKintosh, and D. A. Weitz, J. Cell. Biol. **183**, 583 (2008).
[70] M. F. Copeland and D. B. Weibel, Soft Matter **5**, 1174 (2009).
[71] E. Selander, H. H. Jakobsen, F. Lombard, and T. Kiørboe, Proc. Natl. Acad. Sci. USA **108**, 4030 (2011).
[72] M. H. Sohn, K. W. Seo, Y. S. Choi, S. J. Lee, Y. S. Kang, and Y. S. Kang, Mar. Biol. Biol. **158**, 561 (2011).
[73] J. Yan, M. Han, J. Zhang, C. Xu, E. Luijten, and S. Granick, Nat. Mater. **15**, 1095 (2016).
[74] R. Di Leonardo, Nat. Mater. **15**, 1057 (2016).
[75] D. Nishiguchi, J. Iwasawa, H.-R. Jiang, and M. Sano, New. J. Phys. **20**, 015002 (2018).
[76] Y. Sasaki, Y. Takikawa, V. S. R. Jampani, H. Hoshikawa, T. Seto, C. Bahr, S. Herminghaus, Y. Hidaka, and H. Orihara, Soft Matter **10**, 8813 (2014).
[77] B. Biswas, R. K. Manna, A. Laskar, P. B. S. Kumar, R. Adhikari, and G. Kumaraswamy, ACS Nano **11**, 10025 (2017).
[78] A. Martín-Gómez, T. Eisenstecken, G. Gompper, and R. G. Winkler, Soft Matter **15**, 3957 (2019).
[79] J. Rotne and S. Prager, J. Chem. Phys. **50**, 4831 (1969).
[80] H. Yamakawa, J. Chem. Phys. **53**, 436 (1970).
[81] R. Kapral, Adv. Chem. Phys. **140**, 89 (2008).
[82] G. Gompper, T. Ihle, D. M. Kroll, and R. G. Winkler, Adv. Polym. Sci. **221**, 1 (2009).
[83] R. G. Winkler, P. Reineker, and L. Harnau, J. Chem. Phys. **101**, 8119 (1994).
[84] L. Harnau, R. G. Winkler, and P. Reineker, J. Chem. Phys. **104**, 6355 (1996).
[85] É. Fodor, C. Nardini, M. E. Cates, J. Tailleur, P. Visco, and F. van Wijland, Phys. Rev. Lett. **117**, 038103 (2016).

[86] M. Doi and S. F. Edwards, *The Theory of Polymer Dynamics* (Clarendon Press, Oxford, 1986).
[87] D. L. Ermak and J. McCammon, J. Chem. Phys. **69**, 1352 (1978).
[88] S. P. Singh, G. Gompper, and R. G. Winkler, J. Chem. Phys. **148**, 084901 (2018).
[89] T. Ihle and D. M. Kroll, Phys. Rev. E **67**, 066705 (2003).
[90] C.-C. Huang, A. Chatterji, G. Sutmann, G. Gompper, and R. G. Winkler, J. Comput. Phys. **229**, 168 (2010).
[91] R. G. Winkler and C.-C. Huang, J. Chem. Phys. **130**, 074907 (2009).
[92] S. Poblete, A. Wysocki, G. Gompper, and R. G. Winkler, Phys. Rev. E **90**, 033314 (2014).
[93] S. P. Singh, C.-C. Huang, E. Westphal, G. Gompper, and R. G. Winkler, J. Chem. Phys. **141**, 084901 (2014).
[94] T. Eisenstecken, A. Ghavami, A. Mair, G. Gompper, and R. G. Winkler, AIP Conf. Proc. **1871**, 050001 (2017).
[95] E. P. Petrov, T. Ohrt, R. G. Winkler, and P. Schwille, Phys. Rev. Lett. **97**, 258101 (2006).
[96] L. Harnau, R. G. Winkler, and P. Reineker, J. Chem. Phys. **102**, 7750 (1995).
[97] R. G. Winkler, J. Chem. Phys. **118**, 2919 (2003).
[98] M. Hinczewski, X. Schlagberger, M. Rubinstein, O. Krichevsky, and R. R. Netz, Macromolecules **42**, 860 (2009).
[99] R. G. Winkler, J. Chem. Phys. **127**, 054904 (2007).
[100] F. S. Gnesotto, F. Mura, J. Gladrow, and C. P. Broedersz, Rep. Prog. Phys. **81**, 066601 (2018).
[101] D. G. Grier, Nature (London) **424**, 810 (2003).
[102] A. Terray, J. Oakey, and D. W. M. Marr, Science **296**, 1841 (2002).